Sensors & Actuators: A. Physical 378 (2024) 115825

Contents lists available at ScienceDirect

Sensors and Actuators: A. Physical

journal homepage: www.journals.elsevier.com/sensors-and-actuators-a-physical

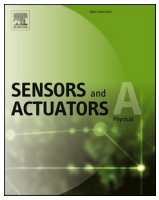

Modular multilayered PVC gel soft actuators for novel lightweight humanoid facial robot

Yi Li [a,b,c,*], Lixiang Zhu [a,b], Ziqian Zhang [a,b], Hangzhong Zhu [a,b], Mingfei Guo [a,b], Zhixin Li [a,b], Yanbiao Li [a,b,*], Minoru Hashimoto [d,**]

[a] Key Laboratory of Special Purpose Equipment and Advanced Processing Technology of Ministry of Education, Zhejiang University of Technology, Hangzhou 310023, China
[b] Zhejiang Provincial Key Laboratory of Special Purpose Equipment and Advanced Processing Technology, Zhejiang University of Technology, Hangzhou 310023, China
[c] Ninghai ZJUT Academy of Science and Technology, Ningbo 315615, China
[d] Faculty of Textile Science and Technology, Shinshu University, 3-15-1 Tokida, Ueda, Nagano 386-8567, Japan

ARTICLE INFO

Keywords:
PVC gel
Soft actuator
Module design
Multilayer
Humanoid facial robot

ABSTRACT

Electroactive multilayered poly (vinyl chloride) (PVC) gel actuators (MPGAs) have attracted increasing interest in the field of soft robotics. However, they still face problems such as relatively low contraction strain, poor durability, and robustness. Herein, we report a new modular multilayered PVC gel actuator (M-MPGA) based on stainless steel meshed electrodes. The output characteristics of the actuator were notably improved by adjusting the plasticizer content in the gel and optimizing the structural parameters of the meshed anode electrodes. The effect of the number of stacked layers on the performance of the actuator was investigated and a dynamic model was derived for the actuator modular design. Actuator modules with multidirectional degrees of actuation were established and applied to a humanoid facial robot for the first time. The developed actuator with a meshed electrode size of #60 was found to exhibit a high contraction strain of over 20 %, which is almost twice that of the traditional MPGAs with an electrode size of #100. In addition, the fabricated actuator module had a low loss rate (1.152 %), high operating bandwidth (9.7 Hz), fast response (~45 ms), and exceptional stability (95.24 % retention at 10,000 s actuation) without any distortion of the actuation performance. Furthermore, the developed prototype humanoid facial robot demonstrated the advantages of ultralight weight (754 g), smooth facial expression, and ease of control.

1. Introduction

With the development of artificial intelligence and 5 G, humanoid expressive robots have been used in areas such as elderly companionship [1], medical care [2], entertainment [3], and interactions [4]. To date, almost all current humanoid facial robots are based on motors and rigid structures [1,5,6], leading to a large mass (typically >3 kg), high noise, and stiff movement [7]. In contrast to conventional rigid actuators, soft actuators are promising artificial muscles to mimic the softness and natural movements of human muscles due to their advantages of large deformation, high flexibility, small size and light weight [8].

To date, many studies have been conducted on humanoid facial robots using soft actuators such as pneumatic actuators (PAs) [9–11], shape memory alloy actuators (SMAs) [12], twisted coil actuators (TCPAs) [13], dielectric elastomer actuators (DEAs) [14], and actuators made of other smart polymer materials [15]. However, humanoid facial robots developed based on soft actuators still face some challenges, such as low integration [15], complex cooperative control [12], and stiff expression effects [12,13]. Moreover, PAs require additional external air sources and control valves, which limits the practical applications of robots [9]. SMAs have problems with slow response as well as a complex net of excessive SMA wires [12], and expression robots using twisted coil actuators (TCPAs) [13] have similar problems. Although facial robots based on dielectric elastomer actuators (DEAs) [14] have a fast response to expressions, they require very high voltages (typically >2 kV), which might pose safety risks and increase the complexity of the control

* Corresponding authors at: Key Laboratory of Special Purpose Equipment and Advanced Processing Technology of the Ministry of Education, Zhejiang University of Technology, Hangzhou 310023, China.
** Corresponding author.
E-mail addresses: ly17@zjut.edu.cn (Y. Li), lybrory@zjut.edu.cn (Y. Li), hashi@shinshu-u.ac.jp (M. Hashimoto).

https://doi.org/10.1016/j.sna.2024.115825
Received 6 July 2024; Received in revised form 11 August 2024; Accepted 19 August 2024
Available online 23 August 2024

system.

On the other hand, PVC gel-based electroactive actuators exhibit many advantages for practical applications in the field of soft robotics, such as fast response (< 50 ms) [16], low driven DC voltage (typically < 0.4 kV (2 V/μm)), and relatively high stress and strain close to human muscle [16]. Li et al. [17] presented a framework of walking assist wear using multilayered PVC gel actuators, obtaining an average decrease of 11 % maximum voluntary contraction (%MVC) of the muscles during walking. Dong et al. [18] designed a 6-degree-of-freedom bionic fish based on multilayered PVC gel actuators, and the maximum swing of the fish tail was 70 mm at 2 Hz voltage. Liu and Zhang [19] proposed a finger orthosis based on a PVC gel actuator with light weight (25 g), fast response (<0.1 s), closed-loop control and correction characteristics. These studies have demonstrated the feasibility of developing expression robots based on PVC gel actuators, which are expected to overcome the shortcomings of expression robots based on soft actuators. Although multilayered PVC gel actuators have been extensively researched, the contraction strain (approximately 10 % [20,21]) is insufficient compared to that of human muscle and remains to be improved, and 40 % attenuation of displacement after multiple drives over 2 hours [20]. For mesh-electrode-based PVC gel actuators, the structure of the mesh anode electrodes and gel structural parameters are only determined based on experience [17], and the relationship between the structural parameters of the actuator and the output characteristics has not been investigated in detail. Consequently, the output characteristics of the actuators were not fully utilized. In addition, no researchers have focused on the effect of the number of stacked layers on the output characteristics of the actuators, which is critical in the design and application of multilayered actuators. Furthermore, the standardized modular design of the soft actuator plays a vital role in enhancing the robustness and flexibility of the actuators in practical applications [16]. However, few of the application studies have designed packaging modules for PVC gel actuators.

Above all, this study aims to resolve the issues of optimizing the characteristics of multilayered PVC gel actuators and designing standardized modules for practical application in humanoid facial robots, as illustrated in Fig. 1. First, the characteristic optimization of the actuator was investigated through material characterization and modeling of the meshed anode parameters. Second, based on the self-weight equivalence principle of the actuators, to investigate the influence law of layer stacking on the output characteristics, a dynamic model of the actuator was established. Subsequently, based on the actuator structure and characteristics, we designed a preload-adjustable package module. Finally, we proposed a novel humanoid facial robot based on the developed modules that can smoothly realize a variety of facial expressions and mimic human facial movements.

2. Results and discussion

2.1. Deforming mechanism of actuators and characteristics of gel membranes

Fig. 2**a** shows the electrodeformation mechanism of the PVC gel actuator. Before energization, the DBA (Dibutyl Adipate, DBA) molecules are distributed irregularly between the PVC molecular chains. After energization, the dipole rotation of the PVC chains rotates Cl ions to the anode side [22] resulting in a high density of DBA molecules on the anode side. The asymmetric distribution of DBA molecules within the gel after energization leads to creep at the anode of the PVC gel, which in turn leads to deformation in the vertical direction [22]. Yamano et al. [23] used mesh anode structures instead of planar anodes to propose a PVC gel actuator based on mesh anodes. As shown in Fig. 2**b**, PVC gel fills into the anode mesh under electrical stimulation (shown in Figure S1**,** Movie S1), which increases the contact area with gel creep, leading to an increase in actuator deformation. The preparation method of the PVC gel is shown in Figure S2. PVC gel membranes with different degrees of plasticization can be prepared by adjusting the mass ratio of DBA to PVC. In this study, the three PVC gels with PVC: DBA ratios of 1:4, 1:6, and 1:8 were denoted as PVC14, PVC16, and PVC18, respectively. We used the scanning electron microscope (SEM) to observe the surface morphology of the PVC14, PVC16, and PVC18 gel membranes (Fig. 2**c**)**.** Briefly, the higher the DBA content, the more pronounced the gel surface fold. As the DBA molecules fill in between the PVC chains, leading to swelling of the gel surface, surface folds are eventually formed after THF evaporation is complete [24]. Furthermore, Figure S3 illustrates the SEM image of the PVC gel membranes without DBA, which has a flat surface and obvious texture, indicating the compact connection between the internal PVC chains. The uniaxial tensile test results for the three gel membranes are shown in Fig. 2**d**. The modulus of elasticity of PVC14, PVC16, and PVC18 is 42, 21, and 14 kPa, respectively, and the elongation at break is 937.85 %, 633.76 %, and 288.12 %, respectively. This is because the DBA molecules filled into the

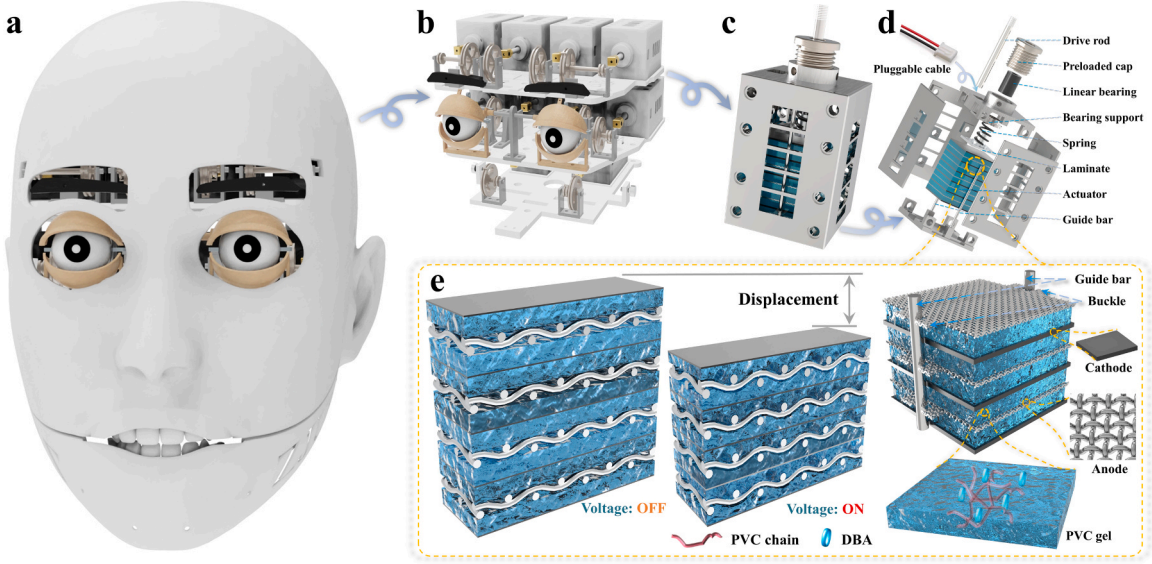

Fig. 1. Illustration of the expression robot based on PVC gel actuators. a) Robot model. b) Robot internal structure. c) PVC gel actuator module. d) Decomposition diagram of the actuator module. e) Multilayered PVC gel actuator structure.

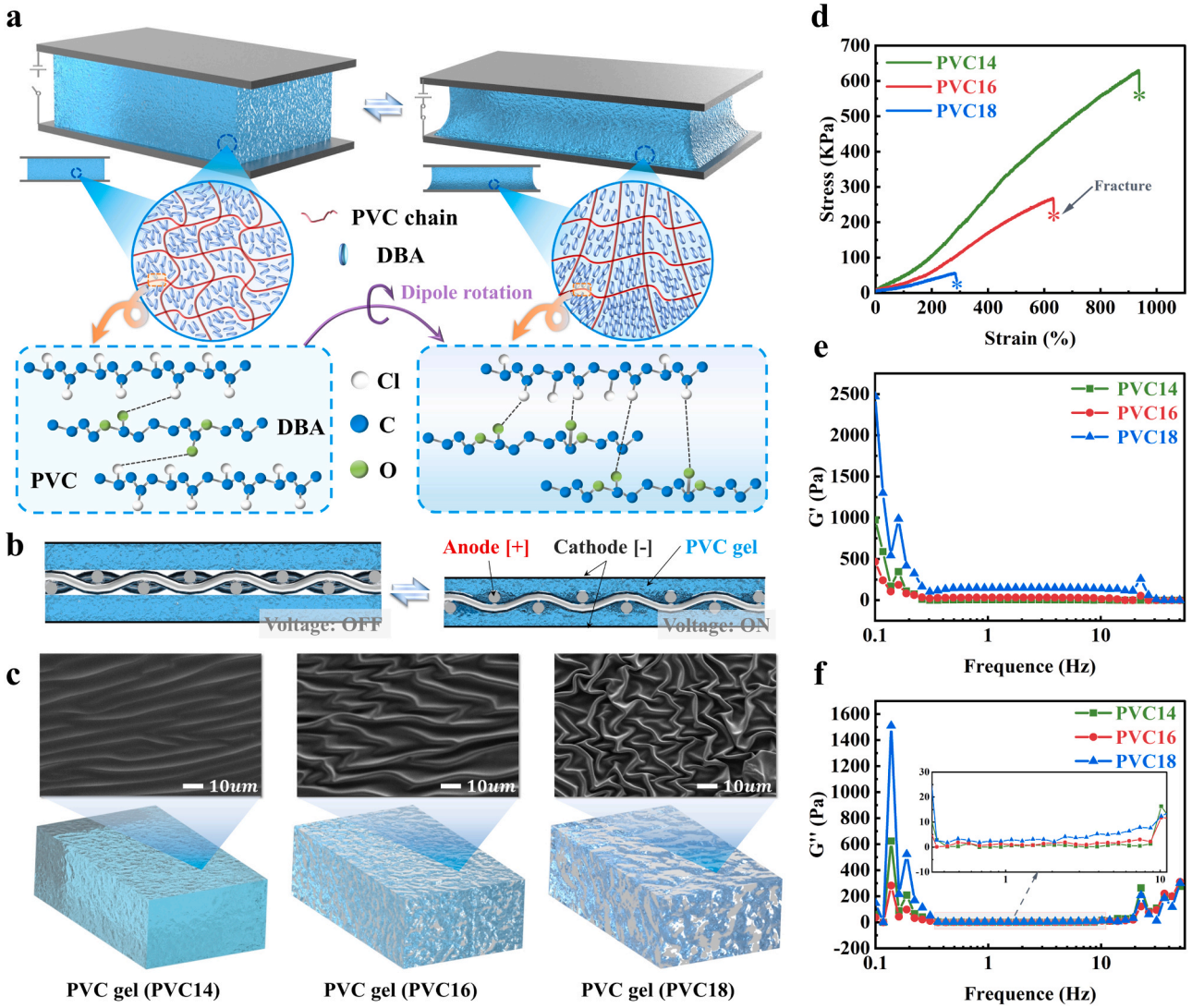

Fig. 2. The PVC gel actuator deformation mechanism and gel material characterization. a) PVC gel actuator creep mechanism. b) PVC gel actuator based on a mesh anode. c) SEM characterization of PVC gels with different DBA contents. d) Uniaxial stretching of PVC gels with different DBA contents. e) PVC gel storage modulus at different DBA contents. f) PVC gel loss modulus at different DBA contents.

PVC chain weaken the inter-chain interaction force. Therefore, the higher the DBA content, the softer are the gel membranes. Figs. 2**e** and 2**f** illustrate the storage modulus and loss modulus with respect to the frequency of the three materials, respectively. At stable frequencies, the viscoelasticity of the material is positively correlated with the DBA content. This is because the filling of the DBA molecules increases the distance between the PVC molecular chains and weakens the degree of PVC gel polymerization, making it easier to deform. We propose a method (Figure S4) for the preparation of MPGAs.

2.2. Optimization of the PVC Gel actuators characteristics

In many studies on PVC gel actuator based on mesh anode [18,25], researchers have often empirically selected PVC gels with different DBA contents and structural parameters for reticulated anodes. Nevertheless, this resulted in not fully utilizing the performance characteristics of the actuators. As a result, it is necessary to investigate different ratios of PVC gels and the structural parameters of reticulated anodes. Considering the small displacement of a single layer actuator, we used 20 × 20 mm, 200 μm thick gel membranes and 10-layer MPGAs (Multilayered PVC gel Actuators, MPGAs) for our experiments. Subsequently, we investigated in detail the various properties of 10-layer MPGAs with different DBA contents and anode structures, including displacement, shrinkage strain, output force, current and frequency responses. We make the following definitions, e.g., #60-MPGAs16 (#60 is the reticulated anode type and 16 is the PVC gel membrane ratio (PVC: DBA)). Fig. 3**a** shows the displacement of MPGAs16 under different reticular anodes. The displacement increases with increasing voltage, but the displacement tends to saturate in the high voltage region. Since the mesh space of the anode is fixed, the creepage space of the PVC gel is limited under electrical stimulation. In addition, the #60-MPGAs16 exhibited greater displacement (1.15 mm) and greater contraction strain (18.3 %, Figure S6a) compared to the #40-MPGAs16 and #100-MPGAs16. To further investigate the impact of anode structure parameters to the displacement characteristics of actuators, we analyzed the results in Fig. 3**a** by establishing an equivalent model of anode structure parameters (Eq. (1), Text S1). The results in Table S2 show that the ξ values of the #60-MPGAs16 are the largest.

$$\xi = \frac{360^{\circ}\cdot 16HL\cdot Strain}{\arcsin\left(\frac{4HL}{L^2+4H^2}\right)\pi^2\left(L^2+4H^2\right)} \tag{1}$$

Where ξ is the creep contact area as a percentage, H is half of the

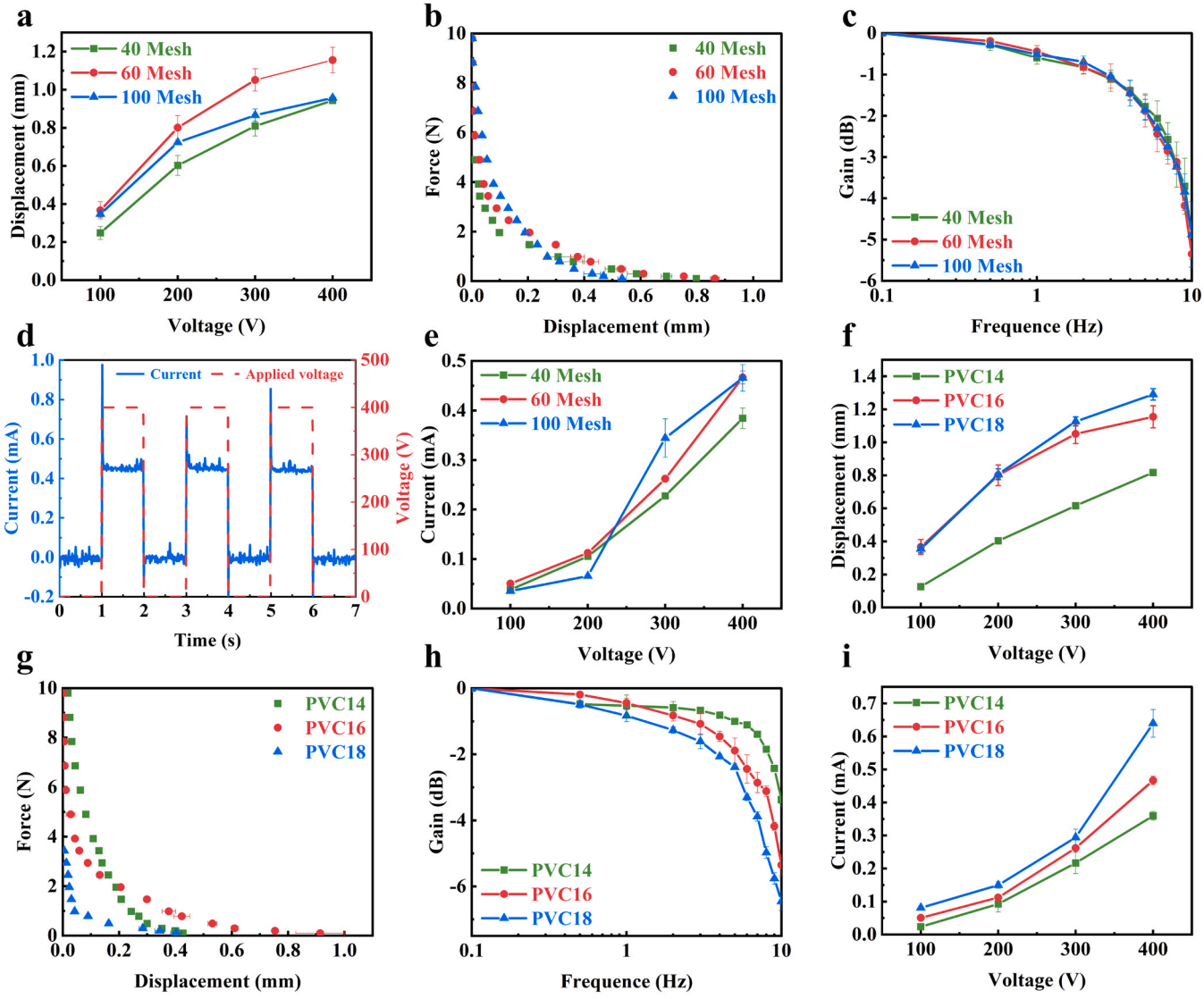

Fig. 3. Optimization of PVC gel actuator characteristics. a) Comparison of 10-layer MPGA16 displacement for different anodes. b) 10-laye MPGA16 output force-displacement comparison for different anodes at 400 V. c) Bode figure of 10-laye MPGA16 frequency response for different anodes at 400 V. d) The current of 10-laye #60-MPGA16 at 400 V. e) Comparison of the 10-laye MPGA16 current with different anodes. f) Comparison of 10-laye #60-MPGA displacements for different DBA contents. g) 10-laye #60-MPGA force-displacement comparison for different DBA contents at 400 V. h) Bode figure of the 10-laye #60-MPGA frequency response for different DBA contents at 400 V. i) 10-laye #60-MPGA current comparison at different DBA contents.

electrode wire diameter, *L* is half of the mesh pitch, *Strain* is the deformation of PVC gel under electric field.

The results in Fig. 3**b** show that when Force > 2 N, the displacement of #100-MPGAs16 is higher than the other. When Force < 2 N, the displacement of #60-MPGAs16 is higher than others. Because the anode mesh pores of the 100 mesh are small and dense, the overall structural stiffness is higher than that of the 60 mesh, as shown in Figure S5. Therefore, the displacement of #100-MPGAs16 is the highest under a high load, whereas the #60-MPGAs16 have a larger displacement relative to the #100-MPGAs16 under a low load. We investigated the displacement response characteristics of the MPGAs16 at different frequency voltages. The experimental results show that the frequency response characteristic of the MPGAs16 is virtually unaffected by the parameters of the mesh anode structure (Fig. 3**c**), while the response time (tc) for all three MPGAs16 is approximately 45 ms (Figure S6b). Consistent with the research findings of Asaka and Hashimoto [26], the current of the #60-MPGAs16 triggers both rising and falling edge responses during each instance of power on and off, respectively (Fig. 3**d**). This shows that the #60-MPGAs16 can be equated to capacitors. When powered on, the actuators were instantaneously charged, and the instantaneous movement of charges within the gel resulted in a rising edge current. After the charges were distributed stably, the current of the actuators tended to stabilize. When powered off, the actuators instantly discharges, generating a falling edge current. We measured the current during the stable period of the #60-MPGAs16 as its working current. The results in Fig. 3**e** indicate that the current of #60-MPGAs16 is independent of the parameters of the mesh anode structure. Fig. 3**f** compares the MPGAs displacement characteristics for the three different DBA contents. The displacement (1.27 mm) and contraction strain (20.45 %, Figure S3c) of the #60-MPGAs18 are higher than those of the other two. After the optimized combination of electrode structure and gel composition in this study, the obtained contraction strain of 10-layer #60-MPGA18 and 10-layer #60-MPGA16 at 400 V are 20.45 % and 18.3 %, respectively, which are about twice as much as that of the conventional #100-MPGA14 strain (10 % [20]). This is due to the fact that, on the one hand, the #60 anode has a larger contact area with the gel creep than the #100 anode (Text S1), and on the other hand, the high DBA content in the PVC18 gel, and the large surface folds deform more

easily, as can be seen in Fig. 2**c**. However, the soft and easily deformable PVC18 gel means that its output displacement under the same load is less than that of PVC14 gel and PVC16 gel, as shown in Fig. 3**g**. Moreover, Fig. 3**g** shows that #60-MPGAs14 can withstand a greater loading force when Force > 2 N, whereas #60-MPGAs16 can achieve a higher output displacement in environments with less than 2 N. These results provide a reference for MPGAs application selection. In contrast to the results of Fig. 2**c**, the results in Fig. 3**h** show that the operating bandwidth (-3 dB) of #60-MPGAs is 9.6 Hz, 7.8 Hz, and 5.6 Hz for PVC14, PVC16, and PVC18 conditions, among others. The viscous modulus of the PVC gels is positively correlated with DBA content (Fig. 2**f**). Therefore, the displacement of #60-MPGAs18 decayed the most (Fig. 3**h**), leading to the longest recovery time (tr) (Figure S6d). As the DBA content increases, the rate of electrical charge movement within the gel enhances accordingly, resulting in a positive correlation between the working current of the MPGA and the DBA content [26] (Fig. 3**i**). Figure S7 shows the output force-displacement curves of the six 10-layer MPGAs at different voltages. In summary, through a comprehensive comparison of multiple output characteristics of MPGAs, it can be determined that the optimal structural parameters for MPGAs are 60 mesh anode and PVC16 gel membranes. Table 1 shows the comparison of the characteristics of the MPGA with those of other soft actuators.

2.3. Deformation characteristics of the MPGAs

To apply and tune the performance of the multilayered actuators, the influence of layer stacking (from 10 to 50 layers) on the output performance of the actuator was investigated. Figs. 4**a** and 4**b** show the displacement and contraction strain of MPGAs, respectively, with respect to the number of stacked layers at different voltages. The displacement growth of the MPGAs is not a fixed multiple of the number of layers, and the contraction strain of the MPGAs decreases as the number of layers increases. To investigate the effect of the number of layers on MPGA, we designed an MPGA equivalent self-weight experiment (Figure S8**)**. The equivalent self-weight experimental group and the actual stacked layers experimental group are denoted as A and B, correspondingly. From Fig. 4**c**, it can be observed that the contraction strain of experimental groups A and B has almost the same decay trend with an increase in the number of layers. Moreover, Fig. 4**b** shows that the change of MPGA contraction strain gradually stabilizes with the stacking of layers, indicating that preloading can make the MPGA structure compact. Under the same loading conditions, the increase in displacement (Fig. 4**d**) and the output work (Fig. 4**f**) of the MPGAs maintains a multiplicative relationship with the increase in the number of layers. The current for the 10-layer #60-MPGAs is 0.445 mA (Fig. 3d), and the mass is approximately 3.6 g. Therefore, the power-to-weight ratio of the 50-layer #60-MPGAs is approximately 49.44 W/kg, and the power consumption is approximately 0.89 W. The curvature of the stress-strain curves of MPGA at any number of layers is almost the same (Fig. 4**e**, Figure S9), which is the same as the results of Li et al. [20]. In Fig. 4**g**, it can be found that the increase in the number of layers improves the frequency response characteristic of the MPGA, and the working bandwidths (-3 dB) are 7.8 Hz, 8.7 Hz, and 9.05 Hz for 10 L, 30 L, and 50 L, respectively. Because layer stacking makes the actuator structure compact, it leads to an increase in the working bandwidth. Furthermore, the number of layers did not affect the response and recovery times of MPGA (Fig. 4**h**). To better describe the dynamic feedback of the multilayer MPGA under load, we modeled the dynamics of the multilayer MPGA based on the Hill muscle model [20] and three-element phenomenon model [27] (Eq. (2)**,** Text S2).

$$y(t) = \left(\frac{F_{ce} - L}{K}\right)\left[1 - e^{-(K/B)t}\right]$$
$$F_{ce} = \frac{a(X_{\max} - b)}{b} - a \tag{2}$$

Where F_{ce} is the effective contraction force provided by the artificial muscle, B and K are the damping coefficients and elasticity coefficients, respectively, y is the contraction displacement, L is the loads. a, b and c are constants. X_{max} is the maximum displacement of the actuator.

Fig. 4**i** shows the dynamic model of the 50-layer MPGA under a 200 g load compared with the experimental results. Obviously, the multilayer MPGA model values are in good agreement with the experimental values, which is instructive for the control of the multilayer MPGA.

2.4. Module design and fabrication of MPGAs

Modular design is of paramount importance for achieving functionality and maintainability, particularly in cases requiring high integration and adaptability to diverse applications. Although MPGAs have been used in wearable devices [17,28], bionic fish [18], and grippers [28], suitable packaging modules for MPGAs have not been designed. To improve the MPGA application locations and standardize the design of expression robots, this study proposes a power-pluggable MPGA packaging module (Fig. 5**a**). Figure S10 shows the disassembly diagram of the MPGA package module (M-MPGA). The upper cover of the module is designed using a PH-2 P terminal header socket. The key component is the preload structure consisting of a preload cap-bearing support--spring-laminate. Different degrees of preload can be realized by adjusting the preload cover. Ensure that the internal MPGAs structure is compact. Figure S12 shows the M-MPGA packaging methodology. The 50-layer M-MPGA mass is 10.5 g (32.8 %), the linear bearing mass is 3 g (9.36 %), the MPGAs mass are 18.5 g (48.8 %), and the space utilization is 87 %. Fig. 5**b** shows the results of the displacement comparison before and after the MPGAs packaging. Owing to the unavoidable preload and friction, the M-MPGA loss at 400 V is 11.78 %. The results in Fig. 5**c** show that the force-displacement curves before and after MPGA packaging are almost the same, and the output work loss of the M-MPGA is only 1.512 % at 400 V (Fig. 5**d**). Fig. 5**e** demonstrates that the working bandwidth (-3 dB) of the M-MPGA is up to the equivalent level of biological muscle, namely, 9 Hz [29]. Because the spring housed in the module enables the MPGAs to recover more quickly from power loss, increasing its working bandwidth after packaging (Figure S13b). The results in Figure S13c show that the encapsulation of the MPGAs have no influence on the reaction rate. It is demonstrated that the friction inside the module does not affect the response time of MPGAs. Nevertheless, many studies have been based on the contraction of MPGAs in the vertical direction. Here, we explore the horizontal operating condition of M-MPGA. In the horizontal characterization study of the M-MPGA, since the direction of the contraction force is perpendicular to gravity, causes

Table 1
Performance comparison of the proposed actuator with other actuators.

Actuator type	Material	Energy source	Strain	Bandwidth	Power consumption	Response time
This work	PVC16 #60	2 V/μm	18.3 %	≥9 Hz	0.18 W (10-layer)	≈ 0.045 s
This work	PVC18 #60	2 V/μm	20.45 %	≥9 Hz	0.26 W (10-layer)	≈ 0.045 s
Conventional PVC gel actuator [20]	PVC14 #100	2 V/μm	10 %	≥9 Hz	0.15 W (10-layer)	≈ 0.045 s
DEA [33]	VHB4905	55 V/μm	62 %	/	/	≈2 s
Pneumatic actuators [34]	/	air	8.5 %	/	/	≥1 s
Magnetic actuators [35]	/	≤10 V	25 %	/	0.9 W	≈ 0.5 s
SMA [36]	/	≤10 V	10–15 %	/	/	≥10 s

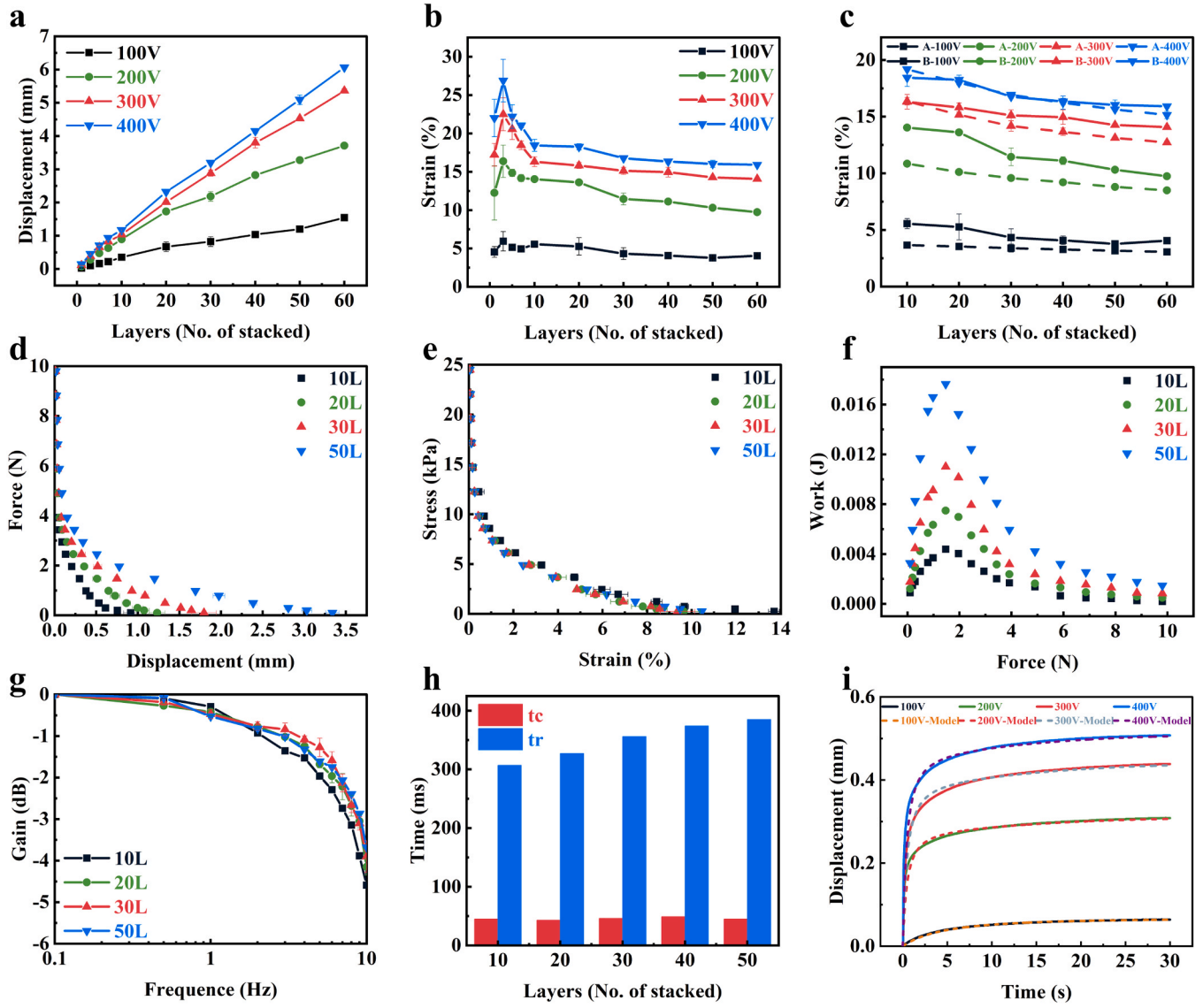

Fig. 4. Multilayered PVC gel actuators characterization. a) #60-MPGA16 displacement with respect to number of layers at different voltages. b) #60-MPGA16 displacement with respect to number of layers at different voltages. c) #60-MPGA16 equivalent self-weight with the actual number of contraction force layers. d) The force-displacement curve of #60-MPGA16 at 400 V. e) Stress-strain curve of #60-MPGA16 at 400 V. f) #60-MPGA16 output work at different numbers of layers. g) Bode figure of the frequency response of #60-MPGA16 at 400 V. h) Number of layers vs. response time (tc) and recovery time (tr) at 400 V. i) Load= 200 g, 50-layer #60-MPGA16 dynamic model compared with the experimental results.

the MPGAs to contract towards the center when energized (Movie S2). This shows that the pretension factor is necessary for the horizontal motion of the M-MPGA, and we defined the pretension factor as shown in Figure S14. When the load is 0.01 N, the M-MPGA with 0 % pretension factor experiences the Movie S2 phenomenon, while a 25 % pretension factor can avoid this phenomenon (Fig. 5**f**). However, an excessively large preload factor can result in significant displacement loss in the M-MPGA. As evidenced in Figure S15a, there is no observable displacement at a preload factor of 100 %. Figs. 5**g** and 5**f** compare the response changes of the M-MPGA under different square, triangular, and sinusoidal voltage signals at 1 Hz. The M-MPGA can respond quickly (~45 ms) under square wave, and it can follow the voltage signals stably and move softly under triangular and sinusoidal waves. In addition, Figure S16 shows the displacement response state of the M-MPGA under three waveforms of 0.2 Hz, 2.5 Hz, and 10 Hz, and Movie S3 shows the dynamic changes of the M-MPGA under different frequencies of sinusoidal waveforms. The M-MPGA produced a very stable displacement distribution in the 1 Hz, 400 V, and 10,000 cycles of the endurance experiments (Fig. 5**j**). After 10,000 cycles, the M-MPGA displacement decreases by only 4.76 %, which is one-tenth the displacement decay of conventional PVC gel actuators (40 % decay at 10,000 cycles) [20]. which greatly enhances the possibility of practical application of PVC gel actuators in soft robots.

2.5. *Proposal and prototyping of a novel humanoid facial robot*

To solve the problems of traditional expression robots, such as high mass, high noise and stiff inter-expression transfer [7,12], we design a new expression robot with lightweight and soft expression based on the proposed M-MPGAs. The robot's design is informed by human ergonomic principles and adhered to the head and face dimensions specified by the Chinese Standards Committee [30], as illustrated in Figs. 6**a** and 6**b**. The right side of Fig. 6**b** shows the eyebrow, eyelid, eyeball, and jaw movement mechanisms from top to bottom. Figure S17 illustrates the appearance and internal structure of the robot in different viewpoints. The human eyebrow movement is mainly powered by the corrugator

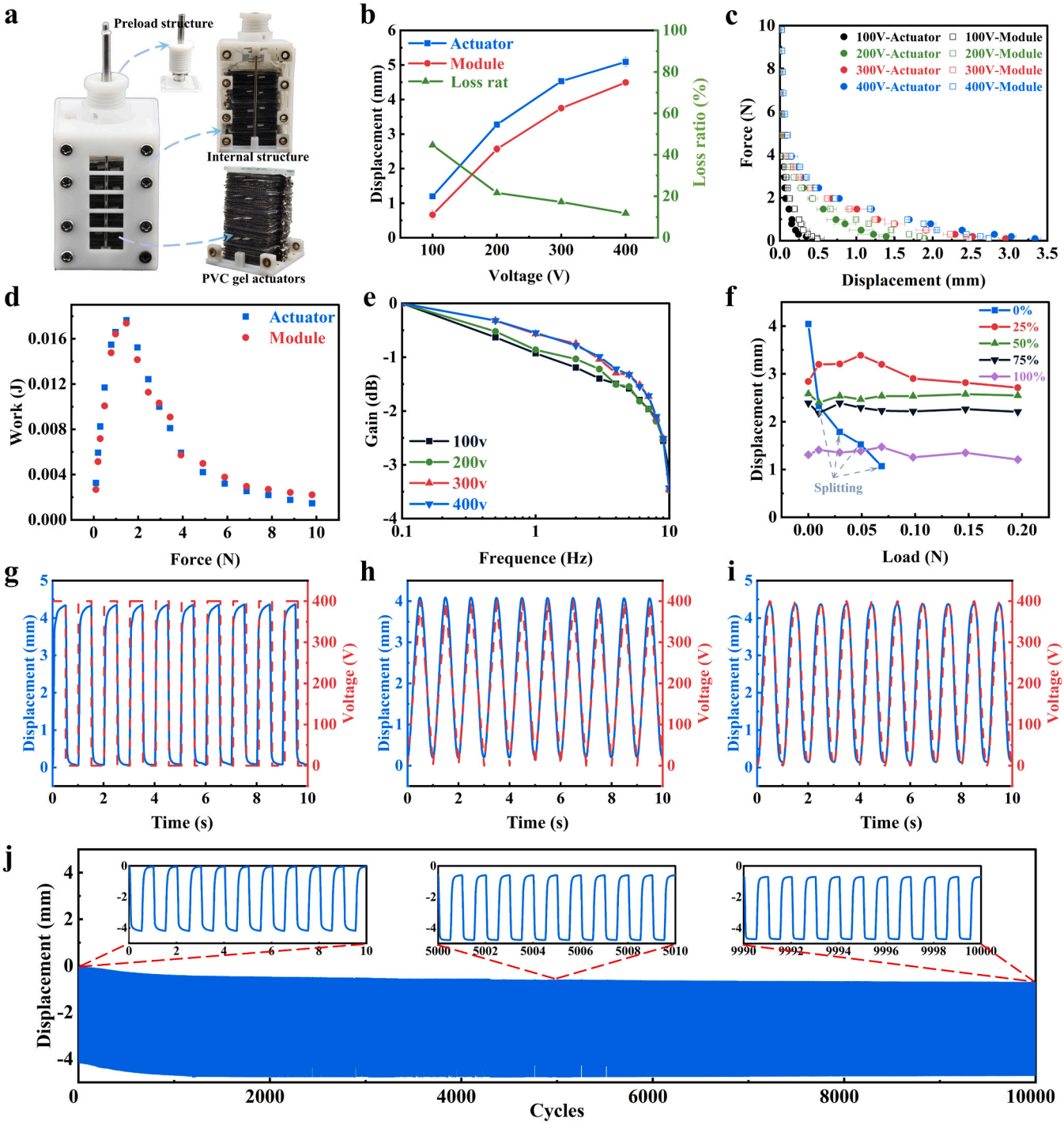

Fig. 5. Design and characterization of M-MPGA. a) The module of MPGA. b) Comparison of displacements before and after MPGA packaging. c) Comparison of output force before and after #60-MPGA16 packaging. d) Comparison of output work before and after #60-MPGA16 encapsulation at 400 V. e) Frequency response Bode curve of M-MPGA. f) M-MPGA leveling test at 400 V with different preload factors. g) M-MPGA response variation at 1 Hz square wave. h) Response variation of the M-MPGA at 1 Hz triangle wave. i) Response variation of the M-MPGA at 1 Hz sine wave. j) Displacement distribution of the M-MPGA over 10000 actuation cycles (about 2.78 h) at 400 V, 1 Hz.

supercilii and depressor supercilii muscles (Figure S18a). We set the caudal end of the corrugator supercilii muscle as the point of rotation of the whole eyebrow, so that the eyebrow makes rotational movements around this point, as shown in figure S18. In daily life, the orbicularis oculi muscle primarily controls the movement of the upper eyelid, enabling eye closure and opening (Figure S19a). Consequently, we designed a single degree of freedom for upper eyelid rotation, defining the amplitude of eyelid rotation as 40°. The upward and downward rotations of the eyeball is effected by the superior and inferior rectus muscles (Figure S20a). We equipped the Hooke's hinge behind the eyeball, and the M-MPGA overcame the gravity of the eyeball and Hooke's hinge to pull the eyeball upward. Downward movement is realized through self-weight. To achieve horizontal rotation of the eyeball, we connected one side of the eyeball to the frame via an elastic wire, while the other side is pulled by the M-MPGA to overcome the elastic force and initiate rotation (Figure S21). Masticatory muscles

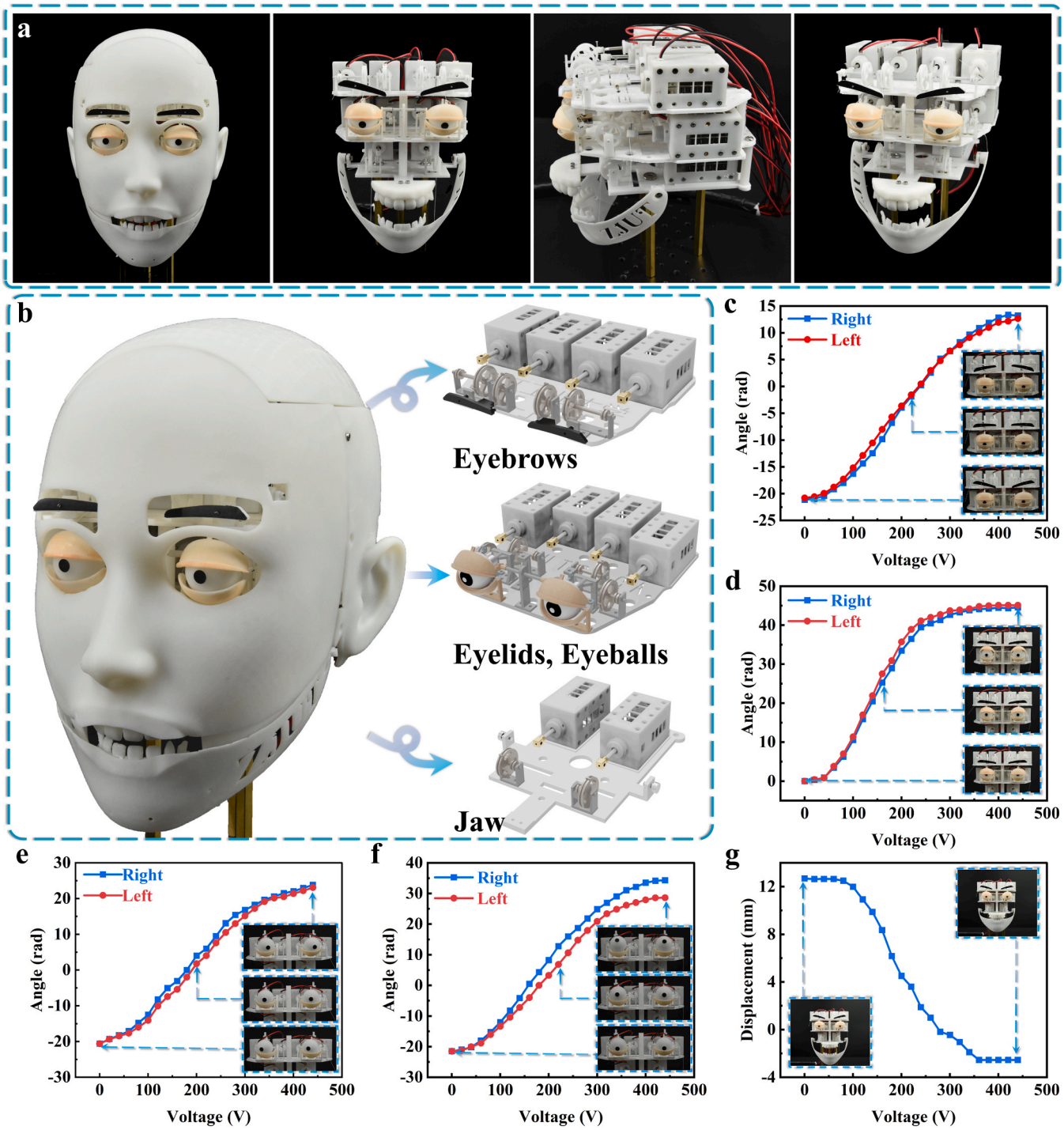

Fig. 6. Overview and characteristics of the fabricated humanoid robot. a) The structural figures of fabrication robot. b) Anatomical figure of the internal structure of the robot. c) Robot prototype and eyebrow, eyelid, eyeball, and jaw structures. d) Eyebrow rotation angle versus voltage. e) Eyelid rotation angle versus voltage. f) Horizontal eyeball rotation angle versus voltage. g) Angle of vertical rotation of the eye versus the voltage. h) Jaw displacement versus voltage.

drive human jaw movements. In this study, the initial state of the jaw is the open stage, and the M-MPGA needs to overcome the self-weight of the jaw to pull the jaw movement, as illustrated in Figure S22. The demand forces and displacements of the eyebrow, eyelid, horizontal eye, vertical eye, and jaw mechanisms were calculated from the Text S3. Assuming that the mechanism rotated at a uniform speed while neglecting friction, we considered a 10 % increase in the displacement and force capacity of the M-MPGA. The parameters of the M-MPGA, outlined in Table S3, were derived from the findings presented in Figs. 5**c** and 5**f**. In addition, Table S3 presents information about the range of motion, desired displacement, and output force of each mechanism. The desired displacement and force are the values that the M-MPGA theoretically needs to provide. The expression robot was employed approximately 560 layers of PVC gel actuators and possesses a mass of roughly 754 g. The dimensions of the robot are 213 mm × 147 mm × 227 mm (length × width × height).

We applied a voltage ranging from 0 to 440 V to the M-MPGAs of the robot's motion mechanisms, with a voltage span of 20 V, and each voltage point is maintained for 5 s. A video camera was used to capture videos of the rotation of the eyebrow, eyelid, eyeball, and jaw.

Subsequently, we processed the rotation angle at each voltage through Image J software. The results in Figs. 6**c**-6**g** show that the ranges of rotation of the horizontal and vertical mechanisms of the eyebrow, eyelid, and eyeball were 35°, 45°, 42°, and 50°, respectively. The jaw opening distance is 12.68 mm (Fig. 6**h**). The insets in Figs. 6**c**-6**h** show the states of each mechanism at voltages of 0, 200, and 440 V. The amplitude of the motion variation remains minimal in the low-voltage region, which is attributed to the preload factor of the M-MPGA. In the high-voltage region, the amplitude of the motion variation is also kept small owing to the saturation effect of the anode mesh. Movie S4 demonstrates the movements of the eyebrow, eyelid, horizontal eye, vertical eye, and jaw, respectively, under sinusoidal waveforms ranging from 1 Hz to 10 Hz. Notably, each of these mechanisms can realize both fast and slow, gentle movements.

2.6. *Emotional expression and application of the robot*

To give the robot emotions, we defined 7 basic expressions for the robot. We design 7 basic expressions based on CK+ data expressions [31] and the facial expression encoding system (FACS) [32]. We used Image J software to measure the rotation angle or the opening and closing values of the eyebrows, eyelids, eyeballs, and jaws for each expression in the CK+ data expressions [31] (Figure S22), and combined them with the FACS [32] to design the parameter values for each movement mechanism of the robot. The final seven facial expressions of the robot are shown in Figure S23. Then, we used Image J to measure the angle and opening/closing values of the motion mechanism in Figure S23, and mapped the motion variation values (Table S4) to the characteristic research results in Figs. 6**c**-6**h** to establish the voltage values of the motion mechanism (Table S5). The results in Figure S16 show that the M-MPGA moves softly under a sine wave and meets the robot response time (0.3 s). Therefore, sinusoidal waveforms were used for the inter-expression transitions. The voltage waveform signals for the eyebrow, eyelid, jaw, and eyeball were designed individually, as depicted in Figs. 7**a**, 7**b**, 7**c**, and 7**d**, respectively. The sequential order of facial expression changes illustrated in Figs. 7**a**-7**c** is as follows: initial state → normal → X → return to the initial state. The sequence of X is disgust, anger, happiness, fear, surprise, and sadness. The eyeballs need to turn downward during the sadness expression, and the other expressions remain horizontal (Fig. 7**d**). We designed the initial state and normal expression to stay for 1 s, and the other expressions to stay for 2 s, with each voltage switching time of 0.3 s. The robot successfully realized seven facial expressions that closely resembled the model, as depicted in Fig. 7**e**. Movie S5 shows the seven facial expression dynamics of the robot. After the 30 participants viewed the expressions of the robot, the average accuracy for the seven expressions is 86.46 % (Figure S24). In addition, the robot can also realize expression movements, such as squinting, rolling eyes, and looking down (Figure S25a).

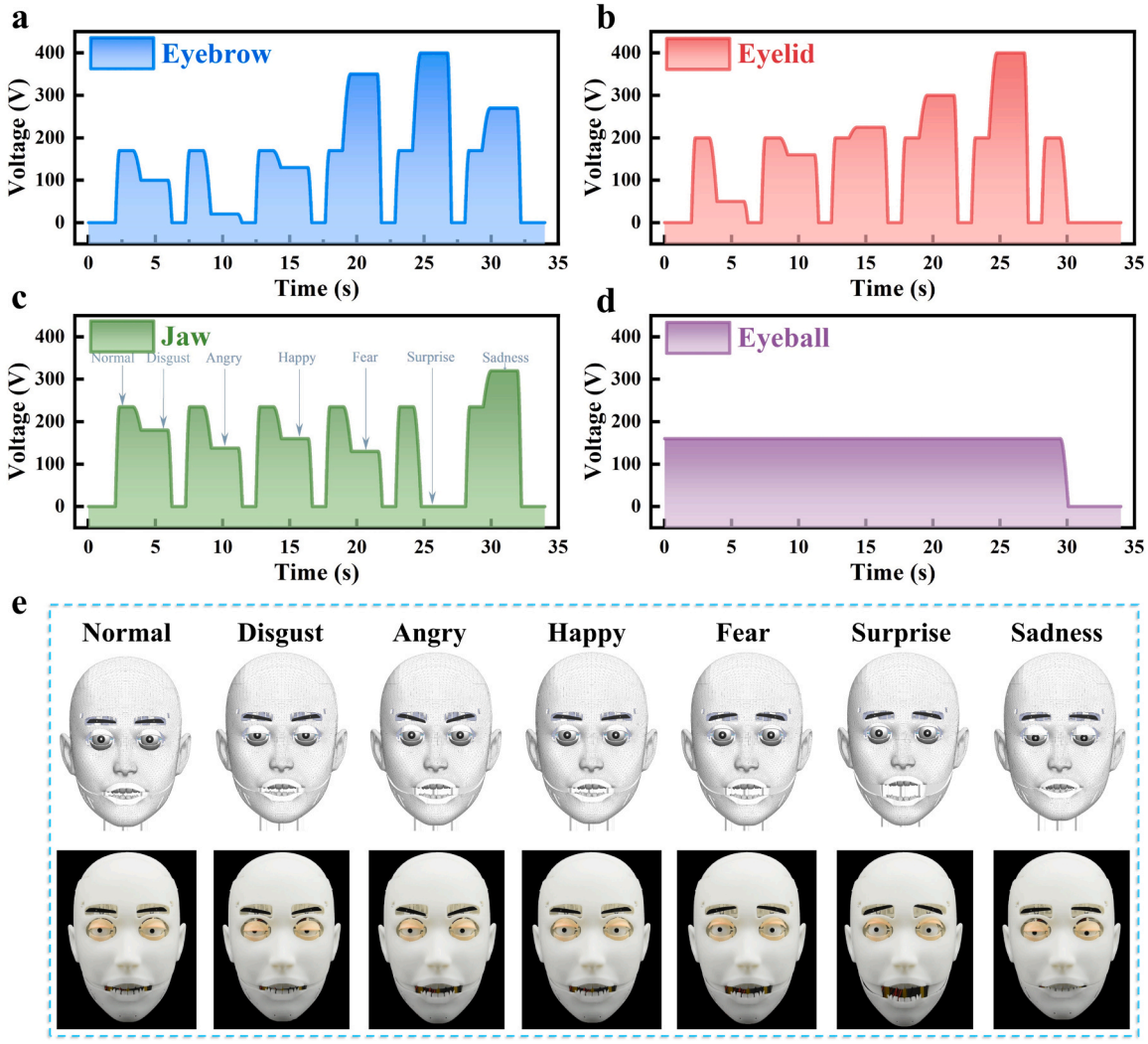

Fig. 7. The 7 basic expression voltage waveforms and expressions. a) Eyebrow voltage waveform. b) Eyelid voltage waveform. c) Jaw voltage waveform. d) Eyeball voltage waveform. e) Seven basic expressions compared to the model.

Movie S6 shows the horizontal, vertical, clockwise, and counterclockwise rotations of the eyeballs of the robot, respectively.

As shown in Fig. 8**a**, the temporal and biting muscles jointly contract to realize jaw closure, and relax to realize jaw opening. Fig. 8**b** demonstrates the motion principle of jaw of the robot. The M-MPGAs are energized to contract, driving the jaw upward, and the jaw relies on gravity to open once the voltage is turned off. The vertical distance between the singer's upper and lower incisors serves as the intended movement distance for jaw of the robot. We intercepted the video frame every 0.16 s and processed the data with Image J, as shown in Fig. 8**c**. Based on the findings presented in Fig. 6**f**, the voltage value for the mandibular M-MPGA was determined, as depicted in Fig. 8**d**. Furthermore, a sinusoidal waveform was employed to design the voltage waveform for the robot's jaw (Fig. 8**e**). Fig. 8**f** shows some of the comparison states of the robot jaw and singer jaw, and Movie S7 shows the real-time states of the robot jaw and singer jaw movements. The result

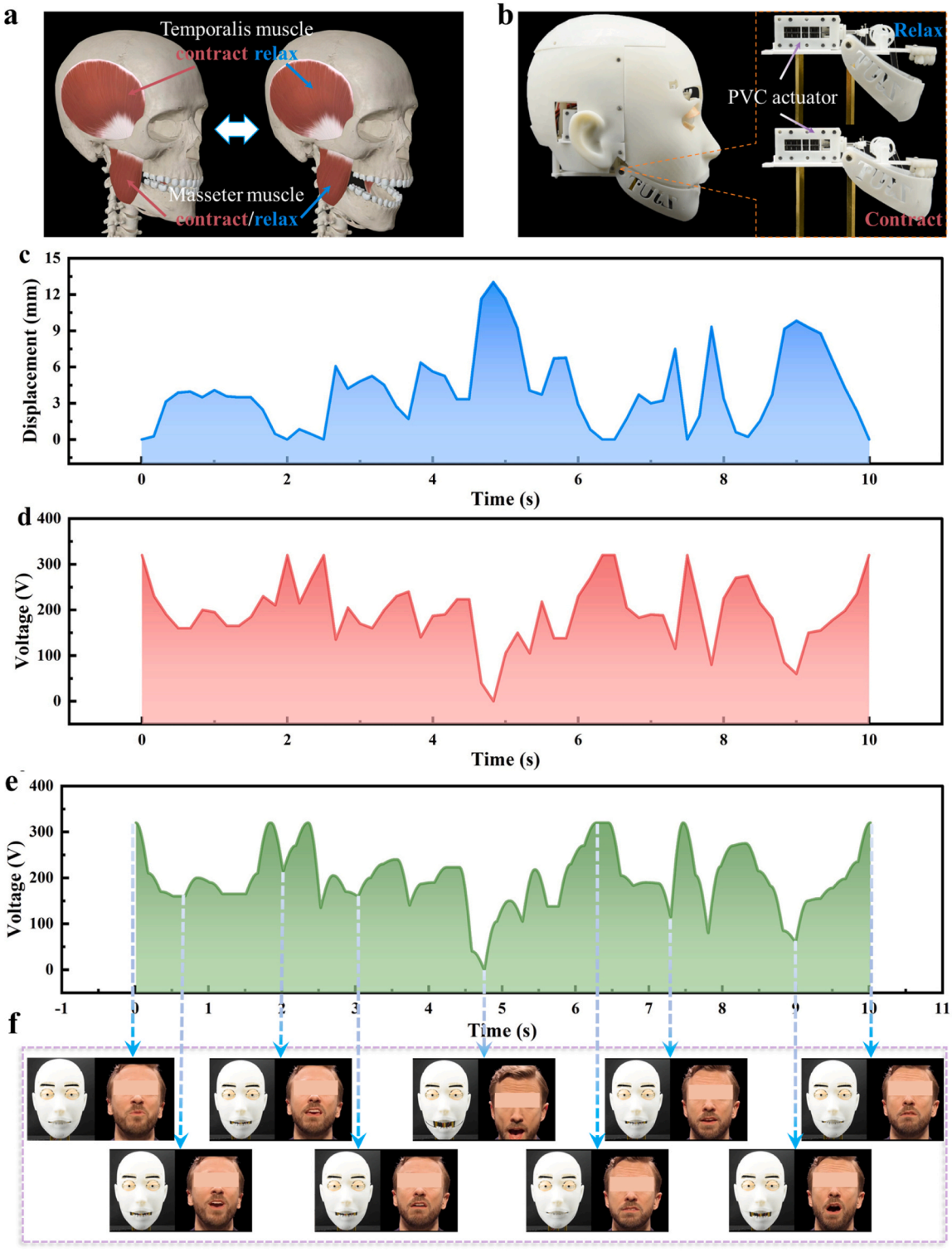

Fig. 8. Robotic jaw application study. a) Anatomy of the jaw muscles. b) Principle of robotic jaw movement. c) Robotic jaw desired displacement. d) Theoretical voltage values of the robotic jaw. e) Robotic jaw voltage waveform. f) Comparison of jaw movement effects.

shows that the M-MPGAs can drive the designed jaw motion, further illustrating that the M-MPGA can imitate the dynamic behavior of natural muscles. The square wave voltage signal was applied to the jaw M-MPGA to enable the robot to execute a rapid biting action. As show in Figures S25b and S25c, the robot bites potato chips and clay (Movie S8), respectively. We found that the response time of the robot jaw biting under a square wave was consistent with Figure S13c (~45 ms). In addition, we preliminarily explored the possibility of robotic applications in the field of roving tracking by manually adjusting the eye actuator voltage waveforms to track car movement (Movie S9).

3. Conclusion

We have developed a modular multilayered PVC gel actuator that has been successfully applied to expression robots. We investigated the effects of DBA content and anode parameters on the output performance to optimize the actuator characteristics. The contraction strain (20 %) of the actuator in this paper is twice that of the results of previous studies. Second, we find that the number of stacked layers can increase the displacement and operating bandwidth of the actuator, and the developed dynamic model of the MPGA fits well with the experimental values. To expand the application environment of the actuator, the designed actuator package module has low loss, fast response, high operating bandwidth, and high durability. Finally, we designed a new robot that has the advantages of light weight (754 g), wide motion frequency (0.1–10 Hz), fast response (~45 ms), and easy control. The robot can easily realize various facial expressions and accurately mimic singer's jaw movements and human bite movements. The results show that the M-MPGA can simulate the dynamic behavior of natural muscles, which confirms the potential of MPGAs for artificial muscles in future robots. The fast response, high-frequency contraction, and low-voltage characteristics of MPGAs suggest their suitability for application in wearable medical devices, haptic sensors, and other fields. Although the actuator can be effectively used for humanoid machine heads, its anode is made of metal mesh material electrodes with relatively high stiffness and weight, which affect the power-to-weight ratio as well as the soft applications. In addition, the output stress is still insufficient compare with that of the human muscle. In future research, we will focus on improving actuator performance and optimizing the modular design for compactness and robustness for multidirectional actuation.

4. Experimental section

Materials: In this study, PVC gel was composed of PVC powder (PVC, CAS 9002–86–2), plasticizer (Dibutyl adipate (DBA), CAS 105997, 96 %) and volatilizer (Tetrahydrofuran (THF), CAS 109999, 99.9 %), both procured from Sigma-Aldrich. All chemicals were used without further purification.

Preparation of PVC gel: Figure S2 shows the preparation method of PVC gel membrane. First, the PVC powder is injected into the THF solution at a uniform speed under a magnetic stirrer. Next, the DBA solution is drained into the THF/PVC mixed solution and centrifuged for 6 min. Then, the three mixed solutions are passed through the coating machine to prepare the prototype of PVC gel membrane. Finally, the PVC gel membrane is obtained after 48 h of THF evaporation.

Characterization: The PVC gel membranes with different DBA contents were characterized using a scanning electron microscope (ZEISS Sigma 300, Germany). The uniaxial tensile mechanical properties of the PVC gel membranes with different DBA contents were tested using an electronic universal testing machine (CMT6103 MTS, USA). The viscoelastic properties of the PVC gel membranes with different DBA contents were tested using an advanced rheometer (SmartPave 92, Austria).

Experimental devices: Figure S26 show the experimental testing devices for displacement, output force, frequency response and current, horizontal characteristics, robot motion mechanism, and robot application research, respectively. Among them, the laser displacement sensor (LK-H050, KEYENCE), high-voltage amplifier (ATA7030, Xi'an Antai Electronic Technology Co., Ltd.), oscilloscope (UTG926E, Unitech Technology Co., Ltd.), NI myRIO (1900, NI), and programmable power supply (D2105P-2000–250, Hangzhou Jiaman Technology Co., Ltd.) were purchased from the official website. (D2105P-2000–250, Hangzhou Jiaman Technology Co., Ltd.) were purchased from the official website, and the rest of the equipment and control circuits were designed by us.

5. Experimental methods

Displacement characteristics: Figure S26a shows the displacement experimental device, using a DC power supply to provide high voltage, and a laser displacement sensor to measure the MPGA vertical displacement data.

Output Force characteristics: As shown in Figure S26b, the MPGAs are energized to apply a load at the end of the pulley, and the data is recorded by the laser displacement sensor after the MPGAs are powered off.

Frequency response and current characteristics: Asaka and Hashimoto [26] demonstrated that the electromechanical model of PVC gel actuators is similar to the capacitor. Considering the problem that the MPGAs cannot be recovered quickly after power failure, this study designs a dual-loop frequency response control circuit as shown in Figure S26c. When the MPGAs are energized, the electromagnetic relay 1 is turned on and the electromagnetic relay 2 is turned off. When the MPGAs are de-energized, the electromagnetic relay 1 is de-energized and the electromagnetic relay 2 is energized. Furthermore, the circuit in Figure S26c can be used to acquire MPGAs current data.

Horizontal output characteristics: The experimental device for testing the horizontal characteristics of the MPGA module is shown in Figure S26d. The M-MPGA is connected to the load via a fixed pulley, and the horizontal output displacement of the M-MPGA is measured under different preload factors and loads.

CRediT authorship contribution statement

Yi Li: Methodology, Formal analysis, Writing – review & editing, Funding acquisition. **Lixiang Zhu:** Investigation, Formal analysis, Writing – original draft, Writing – review & editing. **Ziqian Zhang:** Formal analysis. **Hangzhong Zhu:** Investigation. **Mingfei Guo:** Methodology, Investigation. **Zhixin Li:** Funding acquisition. **Yanbiao Li:** Project administration, Funding acquisition. **Minoru Hashimoto:** Methodology, Funding acquisition.

Declaration of Competing Interest

We declare that we do not have any commercial or associative interest that represents a conflict of interest in connection with the work submitted.

Data Availability

Data will be made available on request.

Acknowledgements

This work was in part supported by Zhejiang Provincial Natural Science Foundation of China (Grant No. LY22E050019 and LGG21E050015), Ningbo Public Welfare Research Program of Ningbo Science and Technology Bureau Foundation of China (Grant No. 2023S066), the National Natural Science Foundation of China (Grant No. U21A20122), and the JSPS (Japan Society for the Promotion of Science) Grant-in-Aid for Scientific Research (C) (Grant No. JP22K04010).

Appendix A. Supporting information

Supplementary data associated with this article can be found in the online version at doi:10.1016/j.sna.2024.115825.

References

[1] Y. Nakata, S. Yagi, S. Yu, Y. Wang, N. Ise, Y. Nakamura, H. Ishiguro, Robotica 40 (2022) 933–950.
[2] G. Pérez-Zuñiga, D. Arce, S. Gibaja, M. Alvites, C. Cano, M. Bustamante, I. Horna, R. Paredes, F. Cuellar, Sensors 24 (2024) 1321.
[3] M. Nakajima, K. Shinkawa, Y. Nakata, IEEE Access 12 (2024) 23930–23942.
[4] Y. Hu, B. Chen, J. Lin, Y. Wang, Y. Wang, C. Mehlman, H. Lipson, Sci. Robot. 9 (2024) eadi4724.
[5] S. Park, H. Lee, D. Hanson, P.Y. Oh, in *2018 15th International Conference on Ubiquitous Robots (UR)*, IEEE, Honolulu, HI, 2018, pp. 511–515.
[6] B. Chen, Y. Hu, L. Li, S. Cummings, H. Lipson, *2021 IEEE Int. Conf. Robot. Autom. (ICRA)*, IEEE, Xi', China (2021) 2739–2746.
[7] L. Yi, Z. LiXiang, Z. ZiQian, G. MingFei, L. ZhiXin, L. YanBiao and H. Minoru,.
[8] H. Hu, D. Li, T. Salim, Y. Li, G. Cheng, Y.M. Lam, J. Ding, J. Mater. Chem. C. 12 (2024) 1565–1582.
[9] T. Hashimoto, S. Hitramatsu, T. Tsuji, H. Kobayashi, 2006 SICE-ICASE International Joint Conference, IEEE, Busan Exhib. Conv. Cent. -BEXCO, Busan, Korea (2006) 5423–5428.
[10] D.F. Glas, T. Minato, C.T. Ishi, T. Kawahara, H. Ishiguro, *2016 25th IEEE International Symposium on Robot and Human Interactive Communication (RO-MAN)*, IEEE, N. Y., NY, USA (2016) 22–29.
[11] D. Yang, W. Sato, Q. Liu, T. Minato, S. Namba, S. Nishida, in *2022 IEEE-RAS 21st International Conference on Humanoid Robots (Humanoids)*, IEEE, Ginowan, Japan, 2022, pp. 542–549.
[12] Y. Tadesse, D. Hong and S. Priya, *Journal of Mechanisms and Robotics*, DOI: 10.1115/1.4003005.
[13] Y. Almubarak and Y. Tadesse, ed. Y. Bar-Cohen, Portland, Oregon, United States, 2017, p. 101631U.
[14] G. Pioggia, A. Ahluwalia, F. Carpi, A. Marchetti, M. Ferro, W. Rocchia and D.D. Rossi, *Applied Bionics and Biomechanics*.
[15] M. Garai, M. Mahato, S. Nam, E. Kim, D. Seo, Y. Lee, V.H. Nguyen, S. Oh, P. Sambyal, H. Yoo, A.K. Taseer, S.A. Syed, H. Han, C.W. Ahn, J. Kim, I. Oh, Adv. Funct. Mater. 33 (2023) 2212252.
[16] Y. Li, M. Guo, Y. Li, J. Mater. Chem. C. 7 (2019) 12991–13009.
[17] Y. Li, Y. Maeda, M. Hashimoto, Int. J. Adv. Robot. Syst. (2015) 1.
[18] C. Dong, Z. Zhu, Z. Li, X. Shi, S. Cheng, P. Fan, Sens. Actuators A: Phys. 341 (2022) 113588.
[19] C. Liu, K. Zhang, IEEE Robot. Autom. Lett. 9 (2024) 3854–3861.
[20] Y. Li, M. Hashimoto, Sens. Actuators A: Phys. 233 (2015) 246–258.
[21] Y. Li, M. Hashimoto, Smart Mater. Struct. 26 (2017) 125003.
[22] M. Ali, T. Ueki, D. Tsurumi, T. Hirai, Langmuir 27 (2011) 7902–7908.
[23] M. Yamano, N. Ogawa, M. Hashimoto, M. Takasaki, T. Hirai, in *2008 IEEE International Conference on Robotics and Biomimetics*, IEEE, Bangkok, 2009, pp. 745–750.
[24] B. Li, Y.-P. Cao, X.-Q. Feng, H. Gao, Soft Matter 8 (2012) 5728.
[25] Z. Liu, B. Li, Y.D. Liu, Y. Liang, Adv. Funct. Mater. 32 (2022) 2204259.
[26] K. Asaka, M. Hashimoto, Sens. Actuators B: Chem. 273 (2018) 1246–1256.
[27] D.B. Reynolds, D.W. Repperger, C.A. Phillips, G. Bandry, Ann. Biomed. Eng. 31 (2003) 310–317.
[28] Y. Li, B. Sun, T. Chen, B. Hu, M. Guo, Y. Li, Jpn. J. Appl. Phys. 60 (2021) 087001.
[29] T. Mirfakhrai, J.D.W. Madden, R.H. Baughman, Mater. Today 10 (2007) 30–38.
[30] ANON.
[31] P. Lucey, J.F. Cohn, T. Kanade, J. Saragih, Z. Ambadar, I. Matthews, 2010 IEEE Computer Society Conference on Computer Vision and Pattern Recognition - Workshops, IEEE, San Francisco, CA, USA, 2010, pp. 94–101.
[32] P. Ekman, E.L. Rosenberg, What the face reveals: basic and applied studies of spontaneus expression using the facial action coding system(FACS) (Second edition), Oxford university press, New York, 2005.
[33] L.J. Romasanta, M.A. Lopez-Manchado, R. Verdejo, Prog. Polym. Sci. 51 (2015) 188–211.
[34] M. Schaffner, J.A. Faber, L. Pianegonda, P.A. Rühs, F. Coulter, A.R. Studart, Nat. Commun. 9 (2018) 878.
[35] P. Boyraz, G. Runge, A. Raatz, Actuators 7 (2018) 48.
[36] Y. Chen, C. Chen, H.U. Rehman, X. Zheng, H. Li, H. Liu, M.S. Hedenqvist, Molecules 25 (2020) 4246.

Yi Li received the M.S. and Ph.D. degrees from Shinshu University, Japan, in 2010 and 2016, respectively. He is currently an associate professor at the College of Mechanical Engineering, Zhejiang University of Technology, Hangzhou, China. His current research interests include artificial muscles and applications in motion-assist systems.

Lixiang Zhu received his bachelor's degree in 2021 from Zhongyuan University of Technology, China. He is currently a postgraduate student at the Zhejiang University of Technology. His research interests include soft actuators and robotics research.

Ziqian Zhang received his bachelor's degree in 2021 from Xiangtan University, China. He is currently a postgraduate student in Zhejiang University of Technology. His research interests include soft electrodes and actuators.

Hangzhong Zhu received his bachelor's degree in 2023 from Zhejiang A&F University, China. Heis currently a postgraduate student in Zhejiang University of Technology. His research interests include soft sensors and actuators.

Mingfei Guo received his master. degree from Shandong University, China, in 2002. He is currently a lecturer at the College of Mechanical Engineering, Zhejiang University of Technology, China. His research interests include soft actuators and robotics.

Zhixin Li received Ph.D. degree from Huazhong University of Science and Technology, China, in 2010. He is currently a lecturer at the College of Mechanical Engineering, Zhejiang University of Technology, China. His research interests include soft actuators and robotics.

Yanbiao Li received his Ph.D. degree from Yanshan University, China, in 2008. He is currently a professor at the College of Mechanical Engineering, Zhejiang University of Technology, China. His research interests include parallel mechanisms, artificial muscles and robotics.

Minoru Hashimoto received M.S. and Ph.D. degrees from the University of Tokyo in 1980 and 1983, respectively. He is currently a specially appointed professor at the Faculty of Textile Science and Technology, Shinshu University. His research interests include artificial muscles and wearable robotics. He is a member of IEEE.